

Particle-in-cell simulations of the Cassini spacecraft's interaction with Saturn's ionosphere during the Grand Finale

Zeqi Zhang ¹*, Ravindra T. Desai ¹*, Yohei Miyake ², Hideyuki Usui ² and Oleg Shebanits ^{1,3}

¹Blackett Laboratory, Imperial College London, SW7 2BW London, UK

²Education Center on Computational Science and Engineering, Kobe University, 657-8501657-8501, 657-8501 Kobe, Japan

³Swedish Institute of Space Physics, SE-752 37 Uppsala, Sweden

Accepted 2021 March 8. Received 2021 March 5; in original form 2021 January 22

ABSTRACT

A surprising and unexpected phenomenon observed during Cassini's Grand Finale was the spacecraft charging to positive potentials in Saturn's ionosphere. Here, the ionospheric plasma was depleted of free electrons with negatively charged ions and dust accumulating up to over 95 per cent of the negative charge density. To further understand the spacecraft–plasma interaction, we perform a three-dimensional Particle-In-Cell study of a model Cassini spacecraft immersed in plasma representative of Saturn's ionosphere. The simulations reveal complex interaction features such as electron wings and a highly structured wake containing spacecraft-scale vortices. The results show how a large negative ion concentration combined with a large negative to positive ion mass ratio is able to drive the spacecraft to the observed positive potentials. Despite the high electron depletions, the electron properties are found as a significant controlling factor for the spacecraft potential together with the magnetic field orientation which induces a potential gradient directed across Cassini's asymmetric body. This study reveals the global spacecraft interaction experienced by Cassini during the Grand Finale and how this is influenced by the unexpected negative ion and dust populations.

Key words: plasmas – space vehicles – planets and satellites: atmospheres – planets and satellites: composition – planets and satellites: individual: Saturn.

1 INTRODUCTION

Spacecraft immersed within a plasma will become electrically charged due to currents of incident electron and ion species (Garrett 1981; Whipple 1981). When the net current induced by these species are not zero, net charge is accumulated and there is a potential difference between the spacecraft and the surrounding plasma. Since the plasma species have different charges, each current is either decreased or increased by the change of the spacecraft potential, which continues until an equilibrium potential is reached, where the net current of all plasma species sum up to zero. Understanding how the spacecraft potential is affected by its environment is important for interpreting the surrounding plasma conditions and on-board plasma measurements that can be significantly affected by the potential difference.

Near a given spacecraft surface a sheath boundary layer screens the potential of the surface over distances of the order of the Debye length (Robertson 2013) and, for sufficiently high relative velocities between the spacecraft and surrounding plasma, a wake of depleted plasma is produced behind the obstacle (Al'pert, Gurevich & Pitaevskii 1966; Ludwig et al. 2012; Miloch 2014). As the spacecraft absorbs incident plasma, a shock is unable to form upstream as would

for an obstacle able to withstand the incoming flow. If the relative velocity exceeds the Alfvénic or acoustic velocities, the associated discontinuities will instead trail downstream and form an approximately conical wake region of disturbed flow commonly referred to as a Mach cone (Willis et al. 2011). Significant asymmetries are introduced into the spacecraft–plasma interaction by the presence of a strong ambient magnetic field which generates a convective electric field in the spacecraft frame (Marklund et al. 1994; Pecseli 2012) and modifies the structure of the wake (Darian et al. 2017; Usui et al. 2019). The high velocities of the significantly lighter electrons compared with ions mean that a spacecraft immersed within a typical space plasma will charge to negative potentials (Spitzer 1941), although processes such as photoelectron and secondary electron emission can shift the potential to positive values (Roussel & Berthelier 2004; Engwall, Eriksson & Forest 2006; Miloch & Vladimirov 2009; Yaroshenko et al. 2011).

When passing through Saturn's ionosphere, the Cassini spacecraft's floating potential was, surprisingly, observed as positive on all encounters below 3000 km altitude (Morooka et al. 2019). The presence of negative ions and dust grains in Saturn's ionosphere is evident from the Langmuir Probe (LP) measurements (Morooka et al. 2019), which showed significant concentrations up to over 95 per cent of the negative charge density, at altitudes of 3200 km down to the closest measurement at ≈ 1600 km. These appear an intrinsic part of the giant planet's ionosphere and distinct from electron depletions associated with Saturn's main rings (e.g. Farrell

* E-mail: zeqi.zhang17@imperial.ac.uk (ZZ); ravindra.desai@imperial.ac.uk (RTD)

et al. 2018) and transient negative ion populations observed near Saturn’s icy satellites (Coates et al. 2010; Desai et al. 2018; Nordheim et al. 2020). Unfortunately, it was not possible to obtain a mass distribution of these negative ions or dust grains due to Cassini’s plasma spectrometers being offline and the Grand Finale plasma data sets therefore lack crucial pieces of information.

A body immersed in a plasma with large quantities of negative ions can attain a positive potential due to the reduced electron currents, as was shown for a dust grain by Kim & Merlino (2006) using orbital motion limit theory, and provides some indication for what might be occurring with Cassini. Similar electron depletions of up to ≈ 96 per cent were, however, observed by Cassini within Titan’s ionosphere, where the spacecraft potential was consistently negative (Wahlund et al. 2005; Cray et al. 2009; Shebanits et al. 2016; Desai et al. 2017b). Significant unknowns therefore remain regarding how spacecraft interact with these outer Solar system plasmas.

Plasmas with a significant negative ion content (ion–ion or dusty plasmas) possess very different characteristics to typical electron–ion plasmas. The reduced mobility of the heavier negative charge carriers alters the electric field screening phenomenon and increases Debye length scales. Plasma conductivities can reverse (Muralikrishna & Kulkarni 2006; Shebanits et al. 2020) and the plasma can host a variety of altered instabilities and wave phenomenon (Shukla & Mamun 2002; Desai et al. 2017a). The interaction of Cassini with Saturn’s ionosphere therefore represents a class of physics quite different to the classic view of spacecraft charging within space plasmas.

In this article, we describe a self-consistent three-dimensional Particle-In-Cell (PIC) study where a model Cassini spacecraft is simulated immersed within plasmas representative of Saturn’s ionosphere as observed during the Grand Finale. Section 2 describes the simulation approach, how Cassini is modelled, and the available measurements of Saturn’s ionospheric plasma. Section 3 then applies these simulations to Saturn’s ionosphere with regards to specific and general parametrizations and conducts a parametric survey to assess the sensitivity of the results to the measured and inferred plasma properties. Section 4 concludes with a summary of the key findings.

2 SIMULATION DEVELOPMENT

2.1 EMSES

The three-dimensional Particle-In-Cell simulation code Electro-Magnetic Spacecraft Environment Simulation (EMSES) has been developed for the self-consistent analysis of spacecraft-plasma interactions on either an electromagnetic or electrostatic basis (Miyake & Usui 2009). The electrostatic version of EMSES is utilized as the typical Alfvén velocities in Saturn’s ionosphere are significantly greater than the spacecraft velocity and in this regime Alfvénic perturbations are assumed to form only a small contribution to the plasma currents (Rehman & Marchand 2014).

Within the PIC approximation (Hockney & Eastwood 1981; Birdsall & Langdon 1985), individual particles are represented by large quantities of ‘super-particles’ that are integrated through the same equations of motion as a real particle (Boris 1970). The plasma is defined to consist of an arbitrary number of plasma species in a drifting Maxwellian velocity distribution to represent in-flowing plasma. Each species has mass and charge normalized to the proton scale with a real ion-to-electron mass ratio. In this study, a negatively charged ion component is included, which is required to study the target plasma environments. The positions of the superparticles are tracked continuously in the simulation box, but the electric and the

magnetic fields are assigned and updated only on the grid points based on the Yee (1966) algorithm, and interpolated on to the super-particles’ positions during calculation. The charge density profile at each time-step is used to solve Poisson’s equation for the electrostatic potential with Dirichlet boundary conditions.

The simulations are run in the spacecraft frame and consists of a three-dimensional box with inflow and outflow boundary conditions along a specified direction of plasma flow, and periodic boundary conditions orthogonal to these. Within the domain the spacecraft is considered as a perfect conductor with separate boundary treatments for both longitudinal and transverse electric fields. The spacecraft surface can accumulate charge caused by impinging superparticles, and redistributes this to ensure the spacecraft is equipotential using the capacity matrix method (Hockney & Eastwood 1981; Miyake & Usui 2009).

2.2 Application to Cassini

2.2.1 Main body

The Cassini spacecraft is a three-axis stabilized spacecraft of approximately 6 m in length. Previous spacecraft charging simulations have considered Cassini in two dimensions (Olson et al. 2010) and as a cylinder in three dimensions during the 2004 Saturn orbit insertion (Yaroshenko et al. 2011). In this study, we model Cassini’s non-uniform shape encompassed within the simulation domain of $12.8 \times 12.8 \times 12.8 \text{ m}^3$, across $128 \times 128 \times 128$ grid cells. Cassini is approximated using three structures: a large thin cylinder representing the antenna dish with an approximated diameter of 4 m and width of 0.55 m, and a longer cylinder representing the main body with an approximated diameter of 2.2 metres and length of 3.8 m. These are separated by a 0.55 metres gap between them, as per the real Cassini spacecraft. Fig. 1 shows a schematic of the simulation geometry, where the X , Y , and Z axes correspond to the $Z_{s/c}$, $X_{s/c}$, and $Y_{s/c}$ axes of the Cassini spacecraft attitude coordinate system, respectively: where X is the direction of main thrusters, Y is opposite to the LP direction, and Z completes the right-hand set (Henry 2002).

The dish and the main body of the spacecraft are considered as a single perfect conductor, as Cassini was designed. Although this approximation does not account for the curvature of the antenna dish, or other instruments attached on to the body, the most important factors for spacecraft charging are the surface area of structures larger than the Debye length scales as well as the ram profile for a fast moving object. As far as the net surface current of the spacecraft and its potential evolution are concerned, this approximation is judged to reasonably approximate dynamics associated with Cassini’s asymmetric shape interacting with Saturn’s ionosphere.

2.2.2 Langmuir Probe

The LP is represented by a small sphere at the side of Cassini, the precise extent of which is defined subgrid. The LP is held at a bias to the main spacecraft, the precise voltage difference specified according to which point in the LP voltage sweeps between -4 V and 4 V that is simulated. The time required for the currents to equilibrate is small compared to the sweep time-scale of 0.5 s (Gurnett et al. 2004), and a fixed bias within the sweep is chosen. The whole Cassini model is floating within the plasma environment and can therefore become charged relative to it but the voltage between Cassini and the probe remains fixed.

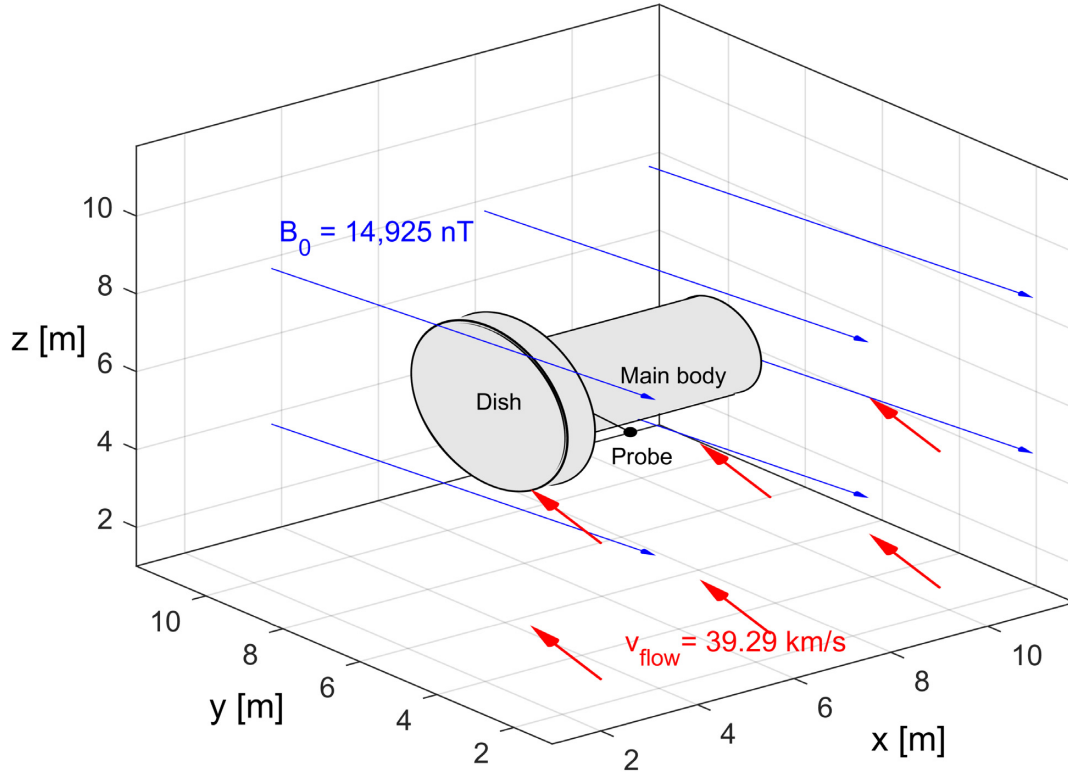


Figure 1. Simulation configuration for Cassini during Grand Finale Rev 292 ingress at 2500 km Saturn altitude. The X, Y, and Z axes correspond to the $Z_{s/c}$, $X_{s/c}$, and $Y_{s/c}$ axes of the Cassini spacecraft attitude coordinate system, respectively, and the precise simulation and plasma parameters are provided in Table 1.

For an LP at a net negative potential within an electron–ion plasma, the total external plasma currents can be considered to derive purely from the positive ion current. This is because the lighter electrons are repelled and therefore their current contribution can be neglected. Similarly, at a net positive potential the external plasma currents is saturated by the faster moving electrons and can be considered to purely consist of electrons. In the presence of large negative ions, however, the situation is different. When the LP is negatively biased, the large negative ions and dust grains are still collected due to their high inertia (mass). At positive biases, the current will be a combination of electrons and negative ions but the significantly smaller electrons still dominate the total current. The simulations are therefore run with the LP biased at a negative potential of -3 V to ensure no electrons are collected as the bias potential is higher than the electron thermal energy. The self-consistent addition of the negative ion component therefore allows us to constrain their contribution to the LP currents and to the overall potential accumulated by the spacecraft.

2.3 Saturn’s ionospheric plasma

Within Saturn’s ionosphere the total current on to the spacecraft is a function of the positive ions, electrons and negative ions, charged dust, secondary electron emission, and photoelectron emission. The photoelectron current at Saturn’s orbit are several orders of magnitude lower than the ion and electron currents (Holmberg et al. 2017; Shebanits et al. 2017), and the secondary electron emission currents are assumed to be of a similar magnitude to this (Morooka et al. 2019). They are therefore not included in this analysis. The simulated currents can therefore be expressed

as

$$I_{\text{total}} = I_{\text{electron}} + I_{\text{ion}^+} + I_{\text{ion}^-}, \quad (1)$$

where I_{ion^+} represents the positive ions and dust, and I_{ion^-} represents the negative ions and dust. While multiple positive and negative plasma components can be included the lack of information on the mass distribution function leads us to use a mean mass to represent these respective components.

2.3.1 Cassini observations

The measured composition of Saturn’s ionosphere provides the inputs to the simulations that produce the currents in equation (1). Post–2012 CAPS was, unfortunately, turned off and the mass distribution on the ambient plasma in Saturn’s ionosphere was therefore unknown. Cassini’s Ion and Neutral Mass Spectrometer was able to provide some information on positive ion composition, but this was limited up to low masses of several amu due to the high spacecraft velocity (Waite et al. 2018). The LP was, however, able to differentiate between the bulk ion, electron, and negative ion currents (Wahlund et al. 2018; Hadid et al. 2019; Shebanits et al. 2020) and therefore provide estimates of their densities (Morooka et al. 2019). The electron density was determined from the positive bias side of the LP sweep (Morooka et al. 2019). The positive ion density could, however, only be constrained as a lower limit due to the unknown mass distribution (Shebanits et al. 2013; Morooka et al. 2019). A lower limit on the negative ion density was therefore also available by assuming quasi-neutrality.

The electron density was observed to increase with decreasing altitude as Cassini sampled denser regions of Saturn’s ionosphere

(Morooka et al. 2019; Persoon et al. 2019). The estimated negative ion density was also observed to increase and at a greater rate than the electrons. As electrons are lost to the negative ions/dust grains, the electron depletion also increased with decreasing altitude, and reached an estimated lower bound of 94 per cent (Morooka et al. 2019). The electron depletion is traditionally quoted as a ratio of negative to positive ion densities such that a 94 per cent depletion corresponds to 6 per cent of the total negatively charged species being electrons, with the rest being negative ions. The LP determined a mean electron temperature of ≈ 0.1 eV and, based upon current balance, an estimate of the minimum mean positive ion mass of ≈ 5 amu at the deepest point sampled (Morooka et al. 2019). The electron temperature was used as a conservative upper limit on the ion temperatures and reducing the ion temperatures below this was later found not to have a significant influence on the simulation results. Within Saturn's ionosphere the spacecraft potential varied between -1.25 and $+0.75$ V with a positive floating potential on every encounter below 3000 km.

2.3.2 Simulation inputs

Rev 292 is selected as a representative flyby with sufficient data from which input parameters are derived. In the first instance, Cassini is simulated at an altitude of 2500 km during ingress where the LP observations revealed an estimated plasma density of 854 cm^{-3} , temperature of 0.093 eV, and the lower bound on the estimated electron depletion was 40 per cent. A higher electron density decreases the Debye length which is the primary constraint on the simulation grid size. This altitude therefore provided an optimal balance between computational load and studying regions of interest with large negative ion concentrations. The magnetic field was measured to be 14 925 nT that results in the electrons being highly magnetized with gyroradii of the order of centimetres and therefore significantly less than the spacecraft size. The positive and negative ions are only weakly magnetized, with gyroradii of tens to hundreds of metres, and therefore much larger than the spacecraft and the simulation domain. Collision frequencies in Saturn's ionosphere are much less than a Herz (Shebanits et al. 2020) and the associated period is significantly greater than the total simulation time of less than a millisecond. During Rev 292, the spacecraft potential was -0.12 V at this altitude, and varied between -0.75 and $+0.65$ V. The precise simulation input parameters are provided in Table 1.

The relative orientation of the spacecraft to the plasma and magnetic field varies very slowly throughout a flyby and is different for different flybys. The simulations described herein do not attempt to produce a precise reproduction of the Cassini measurements, instead attempting to understand the key features of the plasma interaction and associated charge accumulated.

3 RESULTS

3.1 Global interaction

The simulated interaction between Cassini and Saturn's ionosphere is shown at Fig. 2. The left-hand (a–b), centre (c–d), and right-hand (e–f) panels show electron, ion, and negative ion densities, respectively, with the upper (a, c, e) and lower panels (b, d, f), respectively, showing x – y and y – z slices through the simulation. The results are displayed at the end of the simulation run. The two cylinders representing Cassini's antenna dish and main body are apparent as distinct regions absent of plasma. The plasma velocity is arriving pre-dominantly

Table 1. Environmental and system simulation parameters.

| Environmental parameters | |
|---|---|
| Plasma ion density, n_0 | 854 cm^{-3} |
| Negative ion concentration, n_{ni} | 40.2 per cent |
| Ion mass, m_i | 1.4 amu |
| Negative ion mass, m_i^- | 3.0 amu |
| Electron temperature, T_e | 0.093 eV |
| Ion temperature, T_i | 0.093 eV |
| Negative ion temperature, T_i^- | 0.093 eV |
| Magnetic field, \vec{B} | $[1.48\hat{x}, -14.8\hat{y}, 1.24\hat{z}] \mu\text{T}$ |
| Flow velocity, \vec{v}_{flow} | $[-0.189\hat{x}, -37.3\hat{y}, -12.2\hat{z}] \text{ km s}^{-1}$ |
| Alfvén speed, v_A | $11\,149 \text{ km s}^{-1}$ |
| Ion acoustic speed, v_S | 2.56 km s^{-1} |
| Debye length, λ_D | 10.05 cm |
| Electron gyroperiod, τ_{ge} | 2.38 μs |
| Electron plasma period, τ_{pe} | 3.81 μs |
| Ion gyroperiod, τ_{gi} | 6.12 ms |
| Ion plasma period, τ_{pi} | 0.193 ms |
| Negative ion gyroperiod τ_{gi}^- | 13.1 ms |
| Negative ion plasma period, τ_{pi}^- | 0.283 ms |
| System parameters | |
| Grid width, Δr | 10 cm |
| Time step, Δt | 0.033 μs |
| Simulation time, t | 0.67 ms |
| Particles per cell | 20 |
| Domain size | 12.8^3 m^3 |
| Probe bias, ϕ_{LP} | -3 V |

along the y -direction at an angle of $\approx 168^\circ$ to the near-oppositely directed magnetic field. The LP is pointed in the spacecraft ram direction and therefore directly samples the incoming plasma flow. The probe is most visible in Fig. 2(a) at $x = 4$ and $y = 4$ as a local depletion in the electron density due to the negative bias of -3 V.

The high relative velocity of the plasma interaction produces an extended wake of depleted plasma. The length of the wake is greater for positive and negative ions due to their larger inertia resulting in slower refilling. When looking at a slice through Cassini's main body, panels (b, d, f), the wake exhibits the characteristic structure associated with supersonic flow around a cylinder. The slice in the x – y plane, however, in panels (a, c, e) reveals the wake as non-uniform and highly structured behind the antenna dish and the gap between the antenna dish and the main body.

The electron density reveals wing-like structures of enhanced and then depleted density attached to the spacecraft in the y – z plane in panel (b). Similar wing-like structures have been identified at moving bodies produced by Alfvén and whistler waves (Drell, Foley & Ruderman 1965; Neubauer 1980; Stenzel & Urrutia 1989), which propagate at characteristic velocities associated with their relative speed to the spacecraft such that they advect downstream. Electron-wing structures, similar to these reported herein, have been identified as consisting of propagating Langmuir waves (Miyake et al. 2020) produced by electrons reflected from a negatively charged spacecraft which are then guided by the magnetic field lines. Calculation of the LP group velocity, $c_L = \sqrt{3k_B T_e m_e} \approx 1200 \text{ km s}^{-1}$, and the angle to the magnetic field, $\theta = \arctan(v_{\text{flow}}/c_L) \approx 2^\circ$, confirms this mode propagates at small angles to the magnetic field in the spacecraft frame, as can be seen in Fig. 2. Fig. 2(a) shows these wings structures striking the inflow boundary condition and modifying the electron density. Fig. 2(b) however reveals that the effects of this are shifted towards positive z -regions and mostly miss the spacecraft interaction and therefore have a negligible numerical impact. The electron-wings propagate upstream of Cassini and, for flybys where the magnetic

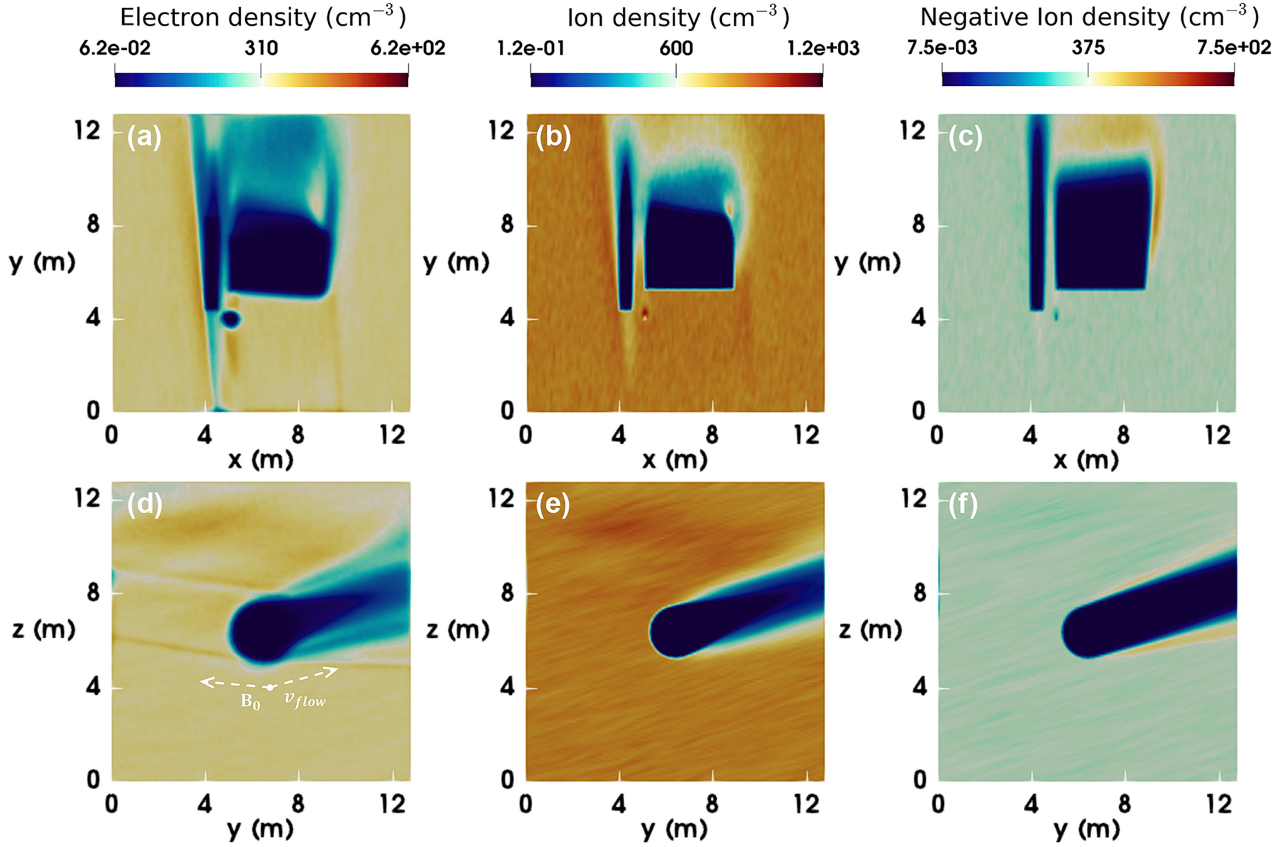


Figure 2. Two-dimensional slices of the electron (a–b), ion (c–d), and negative ion density (e–f) for simulation parameters outlined in Table 1 and described in Section 3.1. The magnetic field is oriented along $1.48\hat{x}, -14.8\hat{y}, 1.24\hat{z}$, and a schematic of the simulation geometry is displayed in Fig. 1.

field is more closely aligned with the spacecraft velocity, they may therefore have influenced the properties of the assumed pristine plasma ahead of Cassini.

Different density distributions are also visible for the different species and the electrons particularly show enhanced spatial variations around the spacecraft. To either side behind the antenna dish in Fig. 2(a) two distinct regions of depleted flows are visible that appears to produce a vortex-type structure in the x - z plane. This is analysed further in Section 3.5.

3.2 Spacecraft potential

In this section, we compare the simulation results to Cassini LP measurements of the spacecraft potential and plasma currents during ingress on Rev 292. Fig. 3 shows the evolution of the spacecraft potential and plasma currents through this simulation run for input parameters derived for when Cassini was at a Saturn altitude of 2500 km in the Northern hemisphere.

The net spacecraft potential is shown in panel (a) and incident plasma currents in panel (b), both of which start near zero. As the spacecraft charges, the main spacecraft body and the probe remain at a fixed bias relative to one another of 3 V. The net current becomes strongly negative before returning to zero when an equilibrium is reached after $\approx 1 \mu\text{s}$. The spacecraft has at this point accumulated a negative floating potential of just under -0.49 V with the probe biased at -3.49 V . The simulation is, however, run for significantly longer to ensure steady state. The simulated potential is -0.42 V and 0.3 V more negative than the observed potential of -0.12 V . The

sensitivity of the spacecraft potential to variations of this magnitude is analysed within following Sections 3.4.

The current decomposition for each of the electrons, positive and negative ions on to each part of the spacecraft is shown in panels (c)–(d). The spike in the negative current in panel (b) corresponds to electron current that also peaks at the beginning of the simulation. The spacecraft surfaces accumulate the associated negative charge and increasingly repel electrons away, thereby reducing the electron current. These initial electron dynamics reflects how the smaller electrons are much more sensitive to the change in the potential of the spacecraft compared to the negative ions which, due to their larger momentum, are not as easily deflected. At the equilibrium potential, all three species of the plasma contribute comparable level of currents on to the spacecraft relative to each other. This current balance is significantly different to within typical electron-ion plasmas, where the electrons constitute the majority of the incident current (Miyake et al. 2020 and references therein). Comparing between the current received from the dish and from the main body, the current composition and relative magnitudes are also different. This is due to the difference in their surface areas but also the deflection of the particle’s trajectories by the ambient magnetic field, resulting in increased quantities of ions and negative ions striking the sides of the dish despite the incident flow being approximately parallel to it.

3.3 LP currents

Fig. 4 shows the currents on to the simulated LP. The positive ion current stabilizes after $\approx 10 \mu\text{s}$ at $\approx 125 \text{ nA}$, slightly lower than the

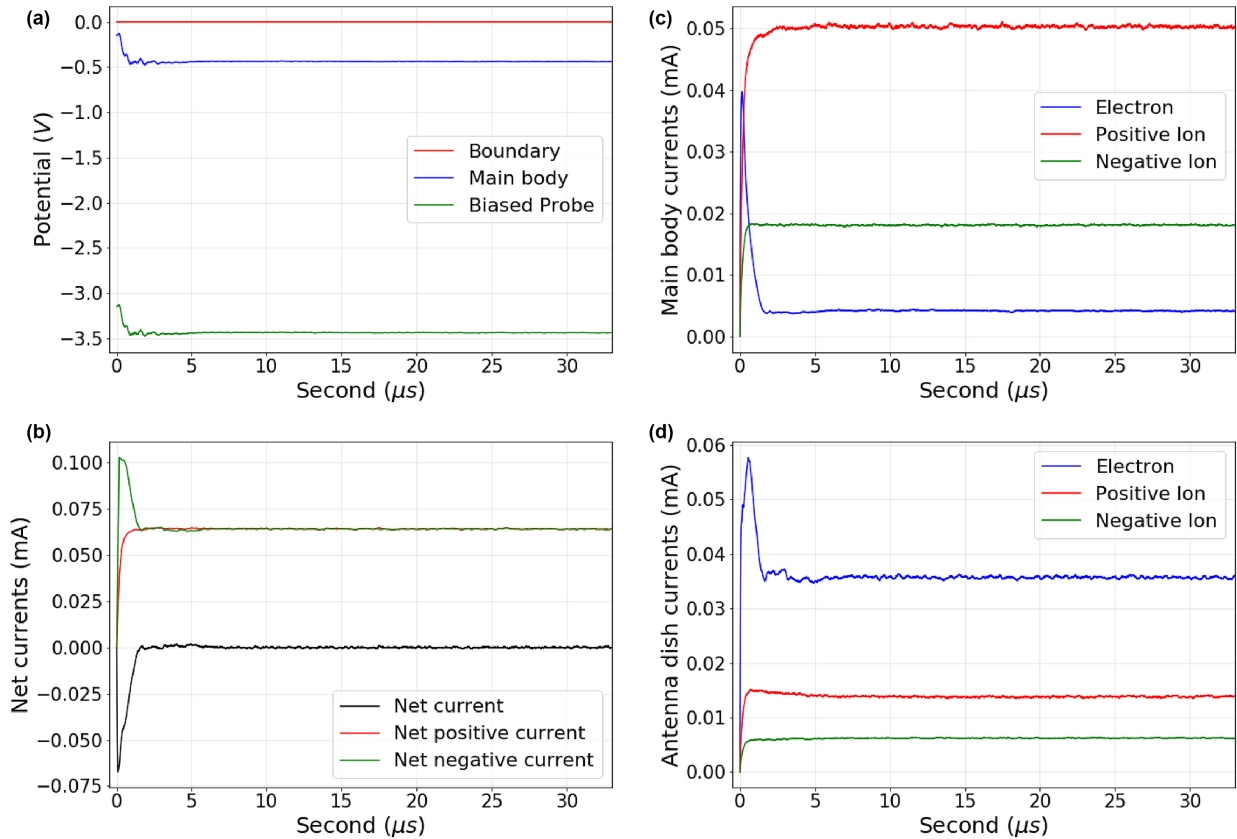


Figure 3. Currents on to the spacecraft within Saturn simulations. (a) Shows the spacecraft potential over time, (b) shows the current on to the spacecraft over time, (c) shows the current on to the dish over time, and (d) shows the current decomposed into the positive and negative parts.

observed total current of ≈ 150 nA. However, when summing the net current over all plasma species, the current is around 30 per cent less. The initial analysis of the LP current was conducted, assuming the total current derived from positive ions and that the negative current was negligible. As a result of the simulation, it is now clear that the negative ion current is not negligible and can be approximated as an almost constant current, regardless of the potential difference, due to

their inertia. These results highlight that while the electron density can be accurately determined, the total plasma density cannot due to the ion and negative ion components. Therefore, by scaling the plasma concentration the net currents on to the probe will increase. There could also be other effects at play such as from the impact and break-up of large dust particles on to the probe and spacecraft that are not included in these simulations.

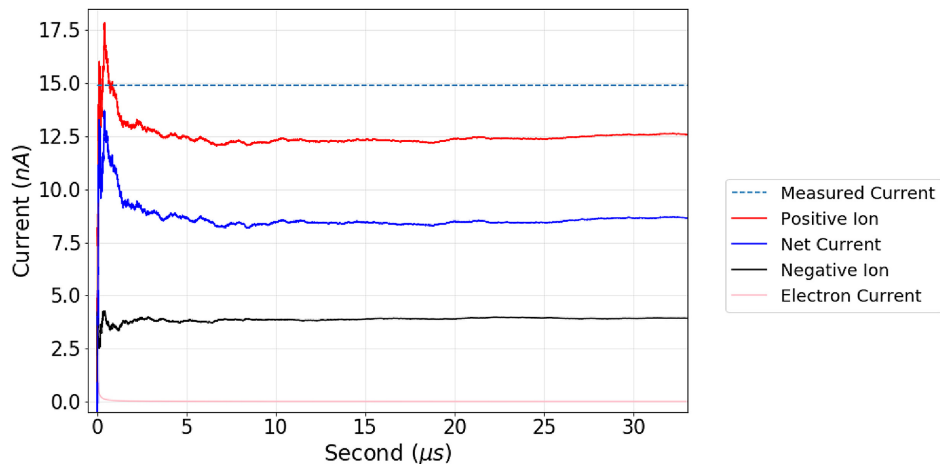


Figure 4. Currents on to the simulated LP decomposed into the positive and negative parts and compared to the Cassini LP readings during Rev 292 at 2500 km altitude ingress.

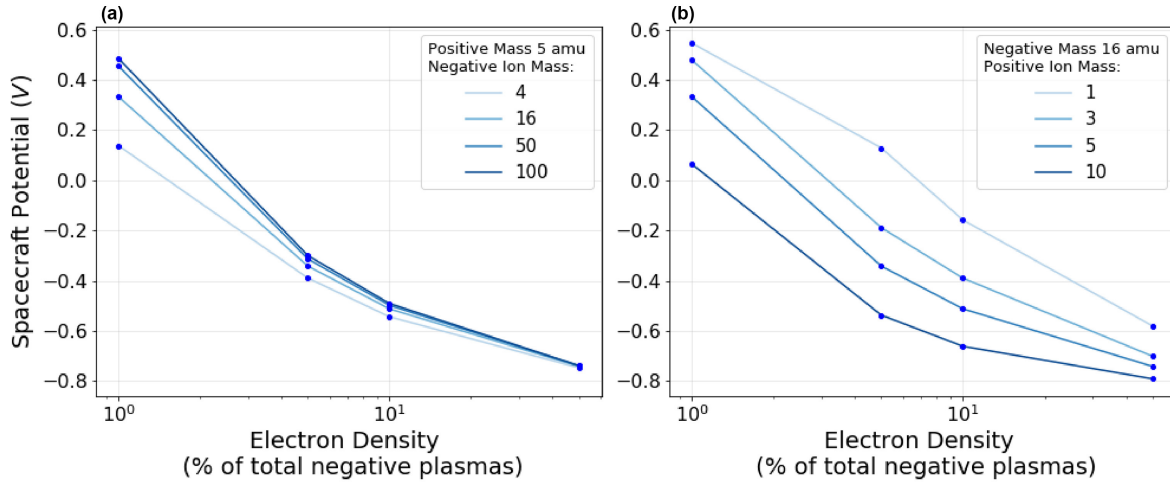


Figure 5. Parametric scan of electron density depletion for a range of negative ion masses (a) and positive ion masses (b).

3.4 Parametric survey

To further understand the sensitivity of the results to the unknown or inferred parameters, we carry out a parametric study and systematically varied the following parameters; the electron depletion, the ion and negative ion masses, the electron temperature and also the ion and negative ion temperatures that were previously assumed to be in thermal equilibrium with the electrons. The total plasma density, however, remains unchanged and the densities are scaled within this. The positive ion mass is now set at 5 amu to represent the measured lower bound in the deep ionosphere (Morooka et al. 2019).

Fig. 5(a) shows the spacecraft potential as a function of electron depletion. The electron density is varied from 1 to 50 per cent of the total ion density for negative ion masses of 4, 6, 50, and 100 amu. For all negative ion masses simulated, as the electron density tends to zero, the spacecraft potential becomes less negative and eventually reaches positive values. For larger negative ion masses the spacecraft become positive at slightly higher electron densities, although this change becomes increasingly smaller with the difference between 50 and 100 amu being significantly smaller than that between 4 and 50 amu.

The effect of a varying positive ion mass on the spacecraft potential is shown in Fig. 5(b), where the negative ion mass is held constant at 16 amu and the spacecraft similarly tends to positive potentials for increased electron depletions. Smaller positive ion masses produced positive potentials at lower masses than larger ones and this change also becomes smaller for the larger masses. The spacecraft potential also appears more sensitive to the positive ion mass than to the negative ion mass. These trends are explained by the variation in the relative mobilities of the positive and negative charge carriers. The production of a positive potential is due to the positive ions actually becoming the most mobile charge carriers which result in the spacecraft accumulating a net positive current. Kim & Merlino (2006) indeed predict that a body immersed in an electron-depleted negative ion plasma can gain a positive potential when the electron density reaches just a few per cent of the total plasma density. Fig. 5(a) indicates this is possible for the Cassini spacecraft in Saturn’s ionosphere.

To study the sensitivity to the electron and ion temperatures, the negative ion mass is held at 16 amu and positive ion mass at 5 amu but the depletion rate is now set at 95 per cent to represent the parameter regime close to where Cassini gains a positive potential. The ion

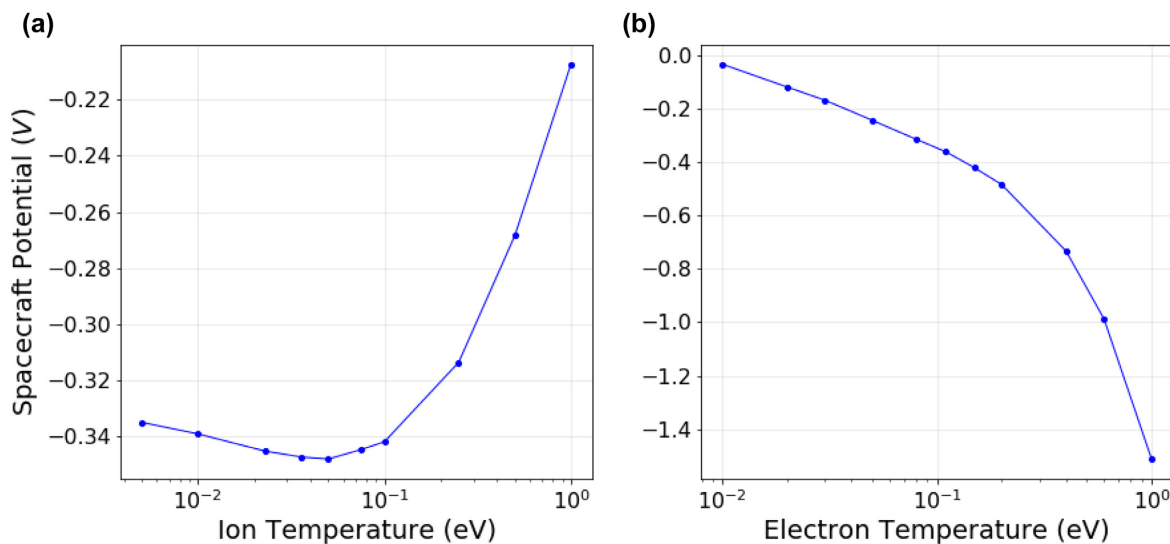


Figure 6. Parametric scan of ion (a) and electron (b) temperatures.

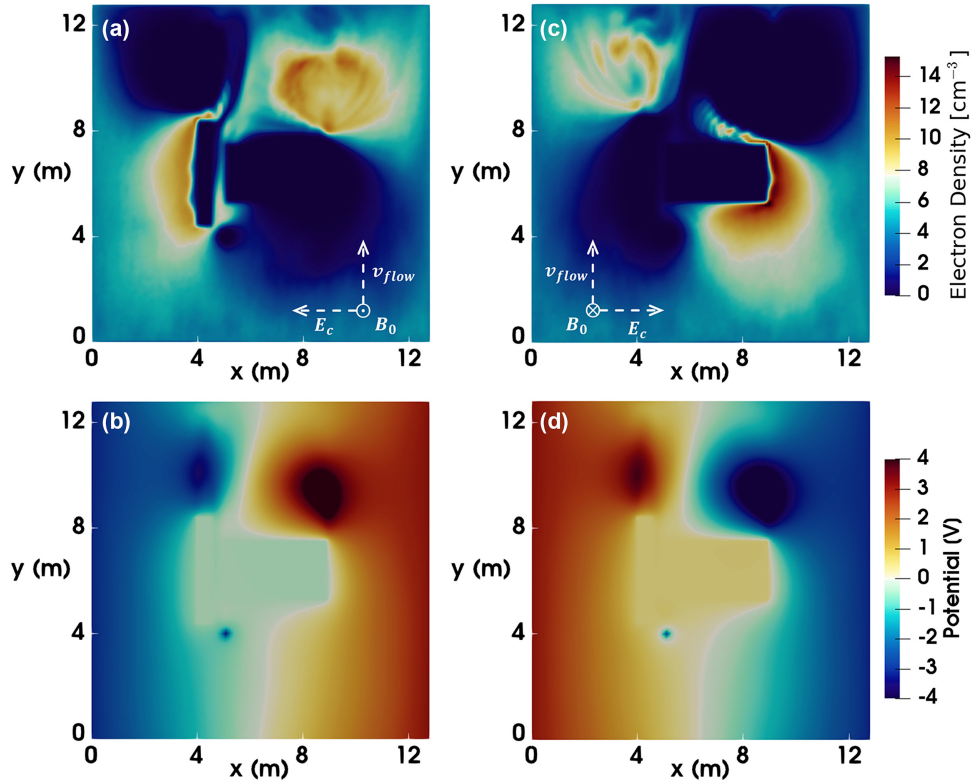


Figure 7. Electron density (a, c) and potential (b, d) of Cassini immersed in a plasma with a negative ion mass of 4 amu and positive ion mass of 5 amu. The left-hand panels (a, b) show the case where the magnetic field is oriented along B_z that produces a spacecraft potential of -0.42 V, whereas the right-hand panels (c, d) show the case with the magnetic field reversed where the spacecraft potential is $+0.38$ V.

temperature variation, shown in Fig. 6(a), reveals that the spacecraft potential increases as the temperature increases from the measured mean temperature of ≈ 0.1 eV, reaching -0.21 V when $T_i = 1$ eV. For temperatures below the measured 0.1 eV, the spacecraft potential initially follows this trend but then, surprisingly, increases again when $T_i \leq 0.5$ eV. This slight effect is attributed to the ions becoming increasingly magnetized as the mean ion gyroradius decreases until it is of a comparable size to the spacecraft. The electron temperature variation, shown in Fig. 6(b), has a much larger impact on the spacecraft potential due to the electron's high relative mobility. The potential consequently varies from -0.05 to -1.5 V, despite the electrons constituting just a few per cent of the total plasma density.

3.5 Potential gradient

The relative mobility of the positive and negative ions explains the positive potential. However, in Fig. 5(a), the spacecraft still charges to a positive potential when using negative ions lighter than positive ions (4 and 5 amu, respectively), so that the negatively charged particles remain the more mobile charge carriers. This therefore appears to contradict this explanation. Beyond the variation in the plasma parameters examined in Section 3.4, the effect of the ambient magnetic field remains to be evaluated.

Within the next simulations the magnetic field direction is oriented perpendicularly to the plasma flow direction, instead along the $+z$ and $-z$ axis. The influence of the magnetic field is felt in the generation of the convective electric field, E_c , in the spacecraft frame, namely,

$$\mathbf{E}_c = -\mathbf{v}_{\text{flow}} \times \mathbf{B}_0, \quad (2)$$

which produces a potential gradient along the main axis of the spacecraft (Pecseli 2012). Fig. 7 shows the electron density and potential within the two simulations with the two different field orientations. The electrons can be seen to be accumulating on one sides of the spacecraft and the potential gradient across the spacecraft interaction is clearly visible. The potential distribution controls where the electrons impact the spacecraft and alters the effective spacecraft cross-section due to Cassini's asymmetric shape. The spacecraft potential is consequently $+0.38$ V in the initial magnetic field configuration, but -0.42 V with the field reversed. Further tests run without the presence of a magnetic field (not shown) also show that the spacecraft is unable to attain a positive potential when the positive ions are less massive than the negative ions.

The perpendicular magnetic field enhances the magnetization of the plasma interaction. The differential electron flows around Cassini can be seen to produce highly structured vortices at a scale that is comparable to Cassini itself. It is interesting to note that electrostatic spacecraft-scale modes have been identified in Saturn's deep ionosphere that are thought to be modulated by Cassini's presence (Sulaiman et al. 2017).

4 CONCLUSIONS

This study simulated the spacecraft–plasma interaction experienced by the Cassini within Saturn's ionosphere during the Grand Finale using a self-consistent three-dimensional PIC code. The asymmetric spacecraft shape was taken into account and an LP was also modelled that enabled preliminary comparisons between the simulated and observed currents.

The global interaction of the Cassini spacecraft was found to be strongly influenced by its asymmetric shape. Differential flows around Cassini's antenna produced a highly structured wake and spacecraft-scale electron vortices behind the spacecraft. Electron-wings associated with propagating Langmuir waves were also identified around the spacecraft that produced a sharp enhancements to the in-flowing electrons. Similar electron-wings were previously identified in simulations of spacecraft moving through the polar regions of the Earth's ionosphere (Miyake et al. 2020) and these simulations indicate this phenomena occurred at Cassini too.

An electron density of 40 per cent of the total negative charge density was initially used in this simulations, which was determined to be a lower bound by Cassini's LP at 2500 km Saturn altitude during Rev 292 (Morooka et al. 2019). The spacecraft potential was found to be negative in the same range as that observed at -0.42 V compared with the observed -0.12 V. The simulations indicated that in Saturn's ionosphere, the ion currents on to the spacecraft and LP were comparable to those from the electrons, a situation unique to plasmas depleted of electrons. The simulated currents on to the LP also revealed that the total currents were in the same range, although slightly lower, than those measured. This is consistent with the 40 per cent electron depletion being a lower bound and indicates that the actual positive and negative ion density may have been higher.

Following these initial simulations a parametric study was carried out to examine how the floating potential is affected by the ambient conditions. To this end, we studied how the spacecraft potential changes with positive and negative ion mass and temperature as well as electron depletion rate. As the electron depletion rate increased the spacecraft potential was observed to become less negative and even attained positive potentials of up to 0.55 V when just a few percent of electrons were contained within the plasma. Varying the plasma masses and temperatures had a similar effect in terms of charge mobility with the electron temperature found to have the largest influence.

The magnetic field orientation was also varied to examine how the induced electric field along Cassini's main axis affected the charge accumulated. The direction of the magnetic field, therefore electric field, produced a strong potential gradient in the potential of the plasma and results in oppositely charge currents preferentially collecting at different parts of the spacecraft. Given the large difference in surface area across Cassini due to its large antenna dish, reversing the magnetic field actually shifted the spacecraft through zero from an initial 0.38 V to negative values of a comparable magnitude of -0.42 V.

As well as providing an insight into the spacecraft plasma interactions experienced by Cassini during the Grand Finale, these simulations have provided an explanation for the positive potentials attained through considering classical charging theory and reversed charge mobility. Despite this, further effects such as secondary electron emission and the break-up of large dust or ice particles on the spacecraft (e.g. Hsu, Horányi & Kempf 2013), and an even more detailed Cassini model incorporating effects such as the curvature of the antenna dish, remain to be constrained. The study does indicate, however, that this approach presents a valuable method for understanding spacecraft charging in the outer Solar system and can assist in interpreting *in situ* measurements of these exotic environments.

ACKNOWLEDGEMENTS

ZZ acknowledges an Undergraduate Summer Research Bursary from the Royal Astronomical Society. RTD acknowledges funding

from NERC grant no. NE/P017347/1. YM and HU acknowledge grant no. 20K04041 from the Japan Society for the Promotion of Science: JSPS, and support from the innovative High-Performance Computing Infrastructure (HPCI: hp200032) in Japan. OS acknowledges RS grant no. RP EA180014 and SNSA grant no. Dnr:195/20. This work has benefited from discussions with International Space Science Institute (ISSI) International Team 437. This work used the Imperial College High Performance Computing Service (doi: 10.14469/hpc/2232).

DATA AVAILABILITY

All simulation data presented in this study can be retrieved from the Zenodo open-access repository at <https://doi.org/10.5281/zenodo.4592954>. Cassini LP data are available from the NASA Planetary Data System archive.

REFERENCES

- Al'pert Y. L., Gurevich A. V., Pitaevskii L. P., 1966, *Am. J. Phys.*, 34, 544
- Birdsall C. K., Langdon A. B., 1985, *Plasma Physics via Computer Simulation*. McGraw-Hill, Inc., New York
- Boris J. P., 1970, *Proceedings of the Fourth Conference on Numerical Simulation of Plasmas*, Technical Report. Naval Research Laboratory, Washington DC, p. 2167
- Coates A. J. et al., 2010, *Icarus*, 206, 618
- Crary F. J., Magee B. A., Mandt K., Waite J. H., Westlake J., Young D. T., 2009, *Planet. Space Sci.*, 57, 1847
- Darian D., Marholm S., Paulsson J. J. P., Miyake Y., Usui H., Mortensen M., Miloch W. J., 2017, *J. Geophys. Res. (Space Phys.)*, 122, 9603
- Desai R. T. et al., 2017b, *ApJ*, 844, L18
- Desai R. T. et al., 2018, *Geophys. Res. Lett.*, 45, 1704
- Desai R. T., Cowee M. M., Wei H., Fu X., Gary S. P., Volwerk M., Coates A. J., 2017a, *J. Geophys. Res. Space Phys.*, 122, 10,408
- Drell S. D., Foley H. M., Ruderman M. A., 1965, *J. Geophys. Res.*, 70, 3131
- Engwall E., Eriksson A. I., Forest J., 2006, *Phys. Plasmas*, 13, 062904
- Farrell W. M. et al., 2018, *Geophys. Res. Lett.*, 45, 8104
- Garrett H. B., 1981, *Rev. Geophys.*, 19, 577
- Gurnett D. A. et al., 2004, *Space Sci. Rev.*, 114, 395
- Hadid L. Z. et al., 2019, *Geophys. Res. Lett.*, 46, 9362
- Henry C. A., 2002, *Space Sci. Rev.*, 104, 129
- Hockney R. W., Eastwood J. W., 1981, *Computer Simulation Using Particles*. McGraw-Hill International Book Company, New York
- Holmberg M. K. G. et al., 2017, *J. Geophys. Res. (Space Phys.)*, 122, 12,258
- Hsu H.-W., Horányi M., Kempf S., 2013, *Earth, Planets and Space*, 65, 149
- Kim S.-H., Merlino R. L., 2006, *Phys. Plasmas*, 13, 052118
- Ludwig P., Miloch W. J., Kählert H., Bonitz M., 2012, *New J. Phys.*, 14, 053016
- Marklund G. T., Blomberg L. G., Lindqvist P. A., Fälthammar C. G., Haerendel G., Mozer F. S., Pedersen A., Tanskanen P., 1994, *Space Sci. Rev.*, 70, 483
- Miloch W. J., 2014, *J. Plasma Phys.*, 80, 795
- Miloch W. J., Vladimirov S. V., 2009, *Geophys. Res. Lett.*, 36, L18110
- Miyake Y., Usui H., 2009, *Phys. Plasmas*, 16, 062904
- Miyake Y., Miloch W. J., Kjus S. H., Pécseli H. L., 2020, *J. Geophys. Res. (Space Phys.)*, 125, e27379
- Morooka M. W. et al., 2019, *J. Geophys. Res. (Space Phys.)*, 124, 1679
- Muralikrishna P., Kulkarni V. H., 2006, *Ann. Geophys.*, 24, 2949
- Neubauer F. M., 1980, *J. Geophys. Res.*, 85, 1171
- Nordheim T. A., Wellbrock A., Jones G. H., Desai R. T., Coates A. J., Teolis B. D., Jasinski J. M., 2020, *Geophys. Res. Lett.*, 47, e87543
- Olson J., Miloch W. J., Ratynskaia S., Yaroshenko V., 2010, *Phys. Plasmas*, 17, 102904
- Pécseli H. L., 2012, *Waves and Oscillations in Plasmas*. Series in Plasma Physics. CRC Press, Hoboken, NJ
- Persoon A. M. et al., 2019, *Geophys. Res. Lett.*, 46, 3061

- Rehman S., Marchand R., 2014, *Phys. Plasmas*, 21, 090701
- Robertson S., 2013, *Plasma Phys. Controlled Fusion*, 55, 093001
- Roussel J.-F., Berthelier J.-J., 2004, *J. Geophys. Res. Space Phys.*, 109, A01104
- Shebanits O. et al., 2016, *J. Geophys. Res. (Space Phys.)*, 121, 10
- Shebanits O. et al., 2020, *Sci. Rep.*, 10, 7932
- Shebanits O., Wahlund J.-E., Mandt K., Ågren K., Edberg N. J. T., Waite J. H., 2013, *Planet. Space Sci.*, 84, 153
- Shebanits O., Vigren E., Wahlund J. E., Holmberg M. K. G., Morooka M., Edberg N. J. T., Mandt K. E., Waite J. H., 2017, *J. Geophys. Res. (Space Phys.)*, 122, 7491
- Shukla P. K., Mamun A. A., 2002, *Introduction to Dusty Plasma Physics*. Institute of Physics Publishing, Bristol; Philadelphia
- Spitzer Lyman J., 1941, *ApJ*, 93, L369
- Stenzel R. L., Urrutia J. M., 1989, *Geophys. Res. Lett.*, 16, 361
- Sulaiman A. H. et al., 2017, *Geophys. Res. Lett.*, 44, 12,049
- Usui H., Miyake Y., Miloch W. J., Ito K., 2019, *IEEE Trans. Plasma Sci.*, 47, 3717
- Wahlund J. E. et al., 2005, *Science*, 308, 986
- Wahlund J. E. et al., 2018, *Science*, 359, 66
- Waite J. H. et al., 2018, *Science*, 362, aat2382
- Whipple E. C., 1981, *Rep. Prog. Phys.*, 44, 1197
- Willis C. T. N., Allen J. E., Coppins M., Bacharis M., 2011, *Phys. Rev. E*, 84, 046410
- Yaroshenko V. V., Miloch W. J., Vladimirov S., Thomas H. M., Morfill G. E., 2011, *J. Geophys. Res. Space Phys.*, 116
- Yee K. S., 1966, *IEEE Trans. Antennas and Propagation*, 14, 302

This paper has been typeset from a $\text{\TeX}/\text{\LaTeX}$ file prepared by the author.